



**HAL**  
open science

# Quantitative characterization of muscle fiber by image analysis

P. Buche, David Mauron

► **To cite this version:**

P. Buche, David Mauron. Quantitative characterization of muscle fiber by image analysis. *Computers and Electronics in Agriculture*, 1997, 16 (3), pp.189-217. 10.1016/S0168-1699(96)00038-5. hal-03079793

**HAL Id: hal-03079793**

**<https://hal.inrae.fr/hal-03079793v1>**

Submitted on 6 Sep 2022

**HAL** is a multi-disciplinary open access archive for the deposit and dissemination of scientific research documents, whether they are published or not. The documents may come from teaching and research institutions in France or abroad, or from public or private research centers.

L'archive ouverte pluridisciplinaire **HAL**, est destinée au dépôt et à la diffusion de documents scientifiques de niveau recherche, publiés ou non, émanant des établissements d'enseignement et de recherche français ou étrangers, des laboratoires publics ou privés.

# Quantitative characterization of muscle fibers

## by image analysis

P. Buche, D. Mauron

Département de Mathématiques et d'Informatique, Institut National Agronomique

laboratoire de biométrie INRA associé

16, rue Claude Bernard, 75231 Paris Cédex 5, France

---

### Abstract

The paper describes a method for measuring a set of quantitative parameters - *structural parameters* (area, perimeter, diameters, shape factors) and *parameters depending on gray-levels* (average luminance and fiber type) in muscle fiber sections. Analysis is performed on a set of serially cut, transverse sections, obtained after a biopsy. A field selected on a serial cutting set is numerized with a CCD black and white video camera. It produces a set of monochrome digital images which are the input data for a model. The method first delineates each fiber section on the image called the reference cutting, calculates the structural parameters and then attempts to follow them on the other images of the set to integrate the other desired parameters -i.e, those depending on gray-levels. The method is semi-automatic. The two main steps - fiber section extraction and fiber section following - are designed to be used on the same principle : first, a completely automatic result is computed using appropriate digital image processing; second, this result is presented to the operator in order to be interactively validated. The software called RACINE - which implements the method - has been used successfully for several years by different laboratories of the French National

22 Institute of Agronomic Research -INRA- on several kinds of animal muscles - pork, chicken,  
23 trout, beef, rabbit, mutton and turkey. The method allows measurements at fibre section scale  
24 on samples as large as several thousand fibres, providing improvements in speed, accuracy  
25 and statistical reliability of analyses. The main applications concern meat quality control  
26 during livestock production and genetic selection.

27

*Keywords:* Image analysis, animal production, quantitative histology, meat quality

---

28

## 29 **1. Introduction**

30

31 Meat quality control is a subject of growing interest for industrial countries where the market  
32 has reached a quantitative saturation point. The French National Institute of Agronomic  
33 Research - INRA - decided to develop research programs in this direction several years ago. In  
34 this context, biologists needed tools to acquire quantitative parameters to describe muscle  
35 from histological material in an objective manner. For example, our method has been used by  
36 biologists to analyze influence of breeding and slaughtering conditions on meat quality in  
37 Fernandez et al (1994).

38

39 Muscle is composed of fibers - 75 to 90 % of the muscle volume - and several tissues. Muscle  
40 fibers are elongated cells several centimeters long and between 20 and 100  $\mu\text{m}$  in diameter. A  
41 muscle is composed of several thousand fibers organized in parallel.

42

43 Meat acidification phenomena after slaughtering have a great importance to explain meat  
44 quality and meat behaviour in industrial processing. For example, post-mortem pH evolution

45 explains 50% of the variability of the transformation efficiency to produce ham. To analyse  
46 meat acidification, biologists study the ATP regeneration mechanism in the fibre. ATP -  
47 adenosine triphosphate - is a molecule which contains the stock of energy of the living cell.  
48 Regeneration is done using the energy found in the food - called glycogen. The regeneration  
49 process can be done by two ways : the glycolitic and the oxidative ways.

50 By the glycolitic way, glycogen is transformed into lactic acid and ATP. By the oxidative way,  
51 glycogen combined with oxygen is transformed into ATP, water and carbon dioxide. After  
52 slaughtering, the oxygen way is stopped, but the glycolitic one continues to work. Due to the  
53 fact that blood circulation is stopped, the lactic acid stays in the cell. Consequently, the post-  
54 mortem regeneration process by the glycolitic way determines the meat acidification.

55

56 Biologists classify cells by histoenzymology in order to determine their behavior in ATP  
57 regeneration. Two kinds of classification are mainly used :

- 58 • revealing SDH activity on a particular cutting. SDH - succinate deshydrogenase - is an  
59 enzyme which permits to identify oxidative cells.
- 60 • revealing ATPase activity at different pH inhibiting or not inhibiting this activity according  
61 to Brooke and Kaiser (1970) or Ashmore and Doerr (1971). ATPase is an enzyme which  
62 transforms ATP in energy. On each cutting, ATPase activity is revealed for only one pH  
63 value. The classification of each fiber is obtained combining the coloration intensity  
64 measured inside the fiber section in different cuttings -i.e for different pH values. In  
65 general, 3 cuttings -i.e 3 pH values- are used to classify the fibers.

66

67 A final fiber classification is obtained integrating SDH or ATPase activities measured on  
68 contiguous cuttings realized perpendicularly to the fiber elongation axis. This is defined as a

69 serial cutting set - see Fig. 1. A transverse section of the same fiber can be found on each  
70 cutting of the set.

71 In a standard serial cutting set, 3 types of cutting are to be distinguished - see Fig. 2:

- 72 • the reference cutting used to delineate the fiber section,
- 73 • the typing colorations used to classify the fibers,
- 74 • the additional parameter cuttings revealing different chemical components. For the  
75 moment, glycogen has been most frequently analyzed because of its great importance in  
76 meat quality determination.

77

78 The biologist's requirement was to have a system which would provide cross-sectional areas  
79 and parameter cutting values for each fiber type. To extract this information from the  
80 histological cuttings, two problems needed to be solved - see Fig. 3 -:

- 81 • fiber section individualization on the reference cutting,
- 82 • fiber section following from the reference cutting to each other cutting of the set to take  
83 account of all the informations describing the same fiber.

84 The objective of our research is to develop a system which permits biologists to treat easily  
85 and rapidly a large sample of fiber sections in order to obtain reliable statistical results.

86 In this paper, a method is proposed which is based on numerical image analysis.

87

## 88 **2. Previous research**

89 Until now, biologists have used different techniques to solve the problem of fiber section  
90 individualization:

- 91 • A first method (Marinova et al (1991)) consists in cutting up with a chisel the fiber sections  
92 on a photograph. The fibers made of paper are then weighed and this information is  
93 converted into area using a calibration relationship between paper weight and fiber area.

- 94 • A second method consists in delineating the fiber sections on a photograph manually using  
95 a cursor on a digital tablet. This system is coupled to a computer which quantifies the areas  
96 (Dudley et al (1983), Wong (1983), Pernus and Erzen (1991)).

97

98 These two methods are used to quantify the fiber section areas but do not solve the problem of  
99 classifying fibers. Usually, each fiber is assigned to a type by a visual analysis of the  
100 photography as in Pernus et al (1986). In other cases, the coloration intensity - information  
101 used to classify the fibers - is measured by a classification based on coloration using  
102 spectrophotomicroscopy as in Bye et al (1989). The system measures the optical density inside  
103 each fiber.

104

105 All these methods allow the desired information to be quantified but they are very time-  
106 consuming because a lot of work must be done manually. Therefore, the analyzed samples are  
107 generally very small: 59 fibers in Bye et al (1989) for instance.

108

109 The development of relatively inexpensive equipment for image capture and processing has  
110 boosted the experimental work using this technique (Jain 1980; Ranft et al 1983; Henckel  
111 1989). A video CCD camera is plugged into a microscope's photo output to obtain a  
112 numerical gray level image representing the observed field. Henckel (1989) proposes a  
113 solution for both problems: fiber section individualization and following. In the  
114 individualization step, he thresholds the gray level (0-255) image interactively to detect the  
115 inter-fiber section network on the reference cutting. Henckel makes the hypothesis that there  
116 is no distortion between cuttings. Therefore the fiber following step is only solved on very  
117 small fields - around 50 fiber sections. The inter-fiber network is stored in the overlay  
118 graphics. A classifying coloration is then put on the microscope. Under video live mode, the

119 operator tries to match the classifying coloration field against the inter-fiber network stored in  
120 the overlay graphics.

121 At the INRA, biologists desire to make experiments on large sets of samples - several  
122 thousand fibers. Therefore, it is very important to design a parameter extraction process which  
123 is as automatic as possible. Henckel's method is very interesting. The interface with the  
124 operator is well-designed, but no special effort has been made to provide automatic tools for  
125 the image analysis step. The analyzed fields are relatively small - around 50 fiber sections -  
126 because the software does not take into account local distortions between cuttings. With our  
127 method, it is possible to process greater fields - between 150 and 300 fiber sections. Manual  
128 interaction is needed only to validate automatic processing for each of the two main steps -  
129 fiber individualization and fiber following. The degree of automation of our software allowed  
130 us to carry out experiments on more than 300 000 fibers - see section 5.5.

131

### 132 **3. Materials**

133

134 The biologist carries out biopsy on the animal - a sample of 0.5 x 0.5 x 1 cm - perpendicular  
135 to the elongation axis of the fibers. The sample is then immediately frozen in liquid nitrogen  
136 and stored at -80°C until histological examination can take place. Several serial 10 µm thick  
137 transverse muscle sections are obtained from each sample with a cryostat at -20°C. For  
138 instance, for the second experiments presented in section 5.5, the biologist prepared four serial  
139 cuttings, one stained in red with azorubine - the reference cutting - , one processed according  
140 to the myosin ATPase technique following preincubation at pH 4.35, one stained for SDH  
141 activity and the last processed to reveal glycogen.

142

143 For image processing, the operational system - see Fig. 4 - consists of an optical microscope  
144 equipped with a CCD black and white camera - Sony XC77CE for instance -, an image  
145 analysis board - Datacell - and a standard workstation computer - Sun 4/75 with 48 Mb central  
146 memory and a color display - running under the Unix system and Motif window manager. The  
147 image analysis board is composed of a graphic memory, an analogue-digital converter linked  
148 to the camera and a digital-analogue converter linked to a display output - monitor - to  
149 visualize images. This board is plugged into the S-bus and driven by the workstation.

150

151 The serial cuttings are numerized sequentially. Each field is represented by a 512 x 512 pixels  
152 image. Each pixel ranges from 0 to 255, according to the luminance measured by the camera.  
153 The reference cutting is first numerized using a green filter to enhance contrast between the  
154 fiber, stained in red, and the unstained inter-fiber material. Large structures belonging to the  
155 interfiber connective tissue network of the reference stain are stored, after a rapid interactive  
156 thresholding, into a graphic memory to match roughly the other stained cuttings. Then, the  
157 operator tries to match in video live mode, as well as possible, these large structures with  
158 those present in the other stained cuttings of the set. Each serial cutting set is available as a set  
159 of images. It will be processed using the methods described in the next section to obtain the  
160 desired parameters.

161

162



## 163 **4. Methods**

164

### 165 4.1 Fiber section extraction step

166

167 The aim is to delineate each fiber section only once, on the reference cutting. On this cutting,  
168 the fiber sections are coloured in black - see Fig. 2. Finding the interfiber network - which is  
169 coloured in white - is equivalent to solving the problem of delineating each fiber section. On  
170 the image, this network can be described as a large size object (hundreds of pixels), composed  
171 of interconnected thin branches. On the whole image, the object/background contrast - i.e.  
172 network/fibers contrast - is important and the illumination intensity is homogeneous - easy to  
173 obtain with microscope lamps -. These two conditions are very important for obtaining  
174 satisfactory results with image analysis. Generally, a real effort must be made to enhance the  
175 staining quality. The azorubine staining used to reveal the interfiber network is red, therefore  
176 the operator uses a green filter to enhance the contrast between fiber and connective tissue.  
177 Lamp light intensity is interactively adjusted on the video monitor to obtain the best possible  
178 interfiber/fibers contrasts.

179 Based on these properties, an automatic algorithm was designed to extract the interfiber  
180 network in two steps: image thresholding and interfiber network branch closing.

181

#### 182 4.1.1 Image thresholding

183

184 Generally, gray level distribution in the image is not bimodal. The thresholding methods based  
185 on the histogram analysis are not appropriate. Inspired by Kolher (1981), the good properties  
186 of object/background contrast and illumination homogeneity have led us to detect the  
187 luminosity on which the average gradient in the whole image reaches the maximum. For each

188 pixel on the image, a discrete approximation of the gradient was computed using the Sobel  
 189 method. For a pixel called \*:

190

$$\begin{array}{ccc} A3 & A2 & A1 \\ A4 & * & A0 \\ A5 & A6 & A7 \end{array}$$

191

192 with A0, A1, ..., A7, its 8 neighbours. The processes to obtain the gradient in X and Y  
 193 directions are:

194

$$195 \quad \text{grad X} = (A1 + 2 A0 + A7) - (A3 + 2 A4 + A5)$$

$$196 \quad \text{grad Y} = (A3 + 2 A2 + A1) - (A5 + 2 A6 + A7)$$

197

198 The gradient amplitude is given by:

199

$$200 \quad \text{grad}(\ast) = (((\text{grad X})^2 + (\text{grad Y})^2) / 32)^{1/2}$$

201

202 Then, for each gray level on the initial image, a computation was made of the average  
 203 associated gradient, accumulating the gradient values of all the positions in the image where  
 204 this gray level was observed. The threshold is chosen as the luminance associated with the  
 205 maximum average gradient - see Fig. 5 -. This threshold computation is global - all pixels of  
 206 the image contribute to its evaluation - which enhances the robustness of the result. The pixels  
 207 of a gray level higher than to this threshold are considered as belonging to the interfiber  
 208 network. Generally, 90% of the interfiber network is obtained using this technique - see Fig. 6  
 209 -. A pretreatment, applied to the initial image before thresholding, enhances the quality of

210 results. A histogram equalization - which is generally used to enhance the contrast for display  
211 purposes - strengthens in our particular application the contrast between fiber sections and the  
212 interfiber network.

213

214 After thresholding, the binary resulting image is not perfect. Artefacts are present in the  
215 interfiber network - dark stains due to coloration in black in Fig. 6 - and inside the fibers -  
216 freezing points in white in Fig. 6. To reduce this noise due to global thresholding, we  
217 eliminate the black connected components of size below 50 pixels - to eliminate holes inside  
218 the fiber sections. This threshold is chosen small , therefore we are sure not to eliminate  
219 connected components belonging to the interfiber network which are in general large  
220 connected components -several thousand connected pixels. In order to close the little broken  
221 branches of the interfiber network, we apply a morphological closing, see Coster and  
222 Chermant (1989), of small size (size of 2).

223

#### 224 4.1.2 Interfiber network branch closing

225

226 At this step, the interfiber network is still not entirely detected. Some long branches - size >  
227 10 pixels - have been lost during global thresholding. To close them, we identify in the  
228 interfiber network image the pixels where the breaks occur. These are called extremity points.  
229 To do so, the interfiber network skeleton image is calculated. Then, from each extremity  
230 point, a possible closing is sought.

231

232 1. Interfiber network skeletization - This homotopic transformation - which preserves  
233 interfiber network connectivity - simplifies the interfiber network structure. All the  
234 branches are 1 pixel width. Therefore, the extremity points are defined as pixels belonging

235 to the skeleton so that the sum of their 8 neighbour pixels is equal to 1 - assuming that  
236 pixels belonging to the skeleton are coded 1 and those belonging to the background 0.

237 2. Possible closing search - First, a short distance closing process was attempted. A point  
238 belonging to the skeleton is sought in a small rectangular neighbourhood - size 10x7 pixels  
239 - starting from the extremity point and oriented in the inertial axis of the opened branch.  
240 The opened branch is defined as the set of 8-connected pixels starting from the extremity  
241 point and ending at the first node of the interfiber network. If a point is found in this  
242 neighbourhood, a segment joining the extremity point and this point is added. After this  
243 process, a more costly long distance algorithm is used to close the larger broken branches.  
244 The idea is to follow the watershed - the central axis of the interfiber network - in the gray  
245 level image starting from the extremity point. A dynamic programming process scans some  
246 possible paths - in the direction given by the inertial axis of the branch - but keeps only the  
247 5 best lanes, maximizing the cumulated luminance intensity in the gray level image -see  
248 Fig. 7 -. The explored lanes may be long - up to 50 pixels in length -. As in the short  
249 distance process, if a point is found, a segment joining the extremity point and this point is  
250 added.

251

252

#### 253 4.1.3 Conclusion on the interfiber network extraction step

254

255 Global thresholding and branch closing steps are completely automatic processes. The  
256 algorithm provides an interfiber network image - see Fig. 8 - that the operator may validate  
257 interactively. Two cases can be distinguished:

258 1. in the first case, the interfiber network is homogeneous in thickness in the entire image.  
259 Then, considering that this interfiber space is artificial - due to azorubine staining which  
260 stretches the interfiber space -, the interfiber skeleton is considered as a good estimation of the  
261 cell borders.

262 2. In the second case, fibers are grouped in bunches which are separated by real interfiber  
263 space - interfiber tissues hierarchically organised. So the operator may merge an intermediate  
264 image - called the big structure image - into the skeleton of the interfiber network image. The  
265 big structure image is a cleaned binary image stored after the global thresholding used during  
266 the automatic step. The operator may also use a graphic tool to delineate and fill interactively  
267 the thick interfiber space

268

269 A graphic editor was also developed to add or remove branches on the interfiber network.

270 When the interfiber network is validated, the morphometrical parameters describing each fiber  
271 section are computed - area, perimeter, diameter. Diameters correspond to the principal axes  
272 of the fibers. These axes are the eigenvectors of the covariance matrix obtained by using the  
273 pixels within the fiber as random variables. The two eigenvectors of the covariance matrix  
274 point in the direction of maximal fiber spread, subject to the constraint that they are  
275 orthogonal.

276

277 4.2 Fiber section following step

278

279 The aim in this step is to locate, in the other cuttings of the set, each fiber section extracted on  
280 the reference cutting. As a first approximation, fibers are considered as nearly cylindrical  
281 objects. It can be affirmed that distortions coming from the biological object - the muscle -  
282 and the experimental technology are negligible compared to the acceptable lack of precision in  
283 the fiber following step. Then, the only geometrical transformation between the reference  
284 cutting and the other cuttings to be superimposed is a combination of rotation and translation -  
285 which are the two degrees of freedom of the microscope. As shown in previous work, Buche  
286 and Camillerapp (1991), this is not sufficient, because local distortions appear between the  
287 serial cuttings, due to different reasons:

- 288 • some adipocyte cells may appear in the interfiber network in one cutting and not in the  
289 others,
- 290 • some fibers may be crushed by the cutting system,
- 291 • some fibers may be contracted or expanded by a particular staining and not by the others.

292

293 Therefore, to solve the fiber following step, it is first necessary to define a geometrical  
294 transformation model adapted to our class of images in order to follow the fiber sections as  
295 precisely as possible. Second, a method must be defined to evaluate the model parameters for  
296 a given pair of images to match.

297

298

#### 299 4.2.1 Geometrical transformation for the fiber following

300

301 The aim in the fiber following step is to measure the luminant intensity observed in the cutting  
 302 to match, either in a little window - 5x5 pixels for instance - centered on the fiber's estimated  
 303 barycenter, or inside a little belt located in the interior border of the fiber section, depending  
 304 on the staining type. This is because some stainings are very homogeneously distributed  
 305 throughout the fiber section - ATPase for instance - and some others reveal an activity mainly  
 306 located on the border of the fiber - like SDH. In the first case, fiber following does not need  
 307 great precision. A geometrical model, which can locate the fiber section barycenter -  
 308 calculated in the reference cutting image - inside the fiber section on the cutting to be  
 309 superimposed, is sufficient. In the second case, each fiber section border - calculated in the  
 310 interfiber network extraction step - must be located as precisely as possible in the coloration to  
 311 match. Consequently, this paper proposes two global transformation models well-adapted to  
 312 each case.

313 When luminant intensity is measured around the fiber's estimated barycenter, we propose a  
 314 **polynomial transformation** because it can take into account one or two local distortions in  
 315 the image field. It is assumed that the coordinates of a set of  $n$  points on the two images to  
 316 match are known :

317

$$318 \quad S_1 = \{ (X_{1i}, Y_{1i}), i \in (1, \dots, n) \} \quad (1)$$

$$319 \quad S_2 = \{ (X_{2i}, Y_{2i}), i \in (1, \dots, n) \} \quad (2)$$

320

321 where  $(X_{1i}, Y_{1i})$  is the point in image 1 which corresponds to  $(X_{2i}, Y_{2i})$  in image 2.

322 If one calls:

$$323 \quad S_2 = \{ (X_{2i}', Y_{2i}'), i \in (1, \dots, n) \} \quad (3)$$

324 the set of points resulting from the application of the polynomial transformation to the set of  
325 points  $S_1$ , the following correspondence is given:

$$326 \quad X'_{2i} = f(X_{1i}, Y_{1i}) \quad (4)$$

$$327 \quad Y'_{2i} = g(X_{1i}, Y_{1i}) \quad (5)$$

328 with  $f$  and  $g$  two polynomial functions of degree  $n$  ( $n \geq 1$ ).

329 Two independent transformations are applied in the  $x$  and  $y$  directions to leave more freedom  
330 to the model. For instance, for  $n=2$ , the  $f$  function is such that:

$$331 \quad X'_{2i} = a_1 + a_2 X_{1i} + a_3 Y_{1i} + a_4 X_{1i} Y_{1i} + a_5 X_{1i}^2 + a_6 Y_{1i}^2 \quad (6)$$

332 The Euclidean distance between the observed points  $(X_{2i}, Y_{2i})$  and the estimated ones  $(X'_{2i},$   
333  $Y'_{2i})$  is defined :

334

$$335 \quad dX_i = (X_{2i} - f(X_{1i}, Y_{1i}))^2 \text{ and } dY_i = (Y_{2i} - g(X_{1i}, Y_{1i}))^2. \quad (7)$$

336 The coefficients  $a_j$  ( $j \in (1, \dots, n)$ ) are calculated in order to minimize the global differences  
337 independently:

$$338 \quad DX = \sum_{i=1}^n dX_i$$

$$DY = \sum_{i=1}^n dY_i$$

339 using the least squares method.

340 The second solution proposes a **thin plate spline transformation** which holds in the model  
341 more information about the local distortions than the polynomial transformation. This model



342 has been presented by Bookstein (1989) and applied on lateral cephalograms - X-rays images  
 343 of the head from the side. The  $\underline{f}$  and  $\underline{g}$  functions are now defined as thin plate spline functions.

344 Equation (6) is replaced by the following:

345

$$346 \quad X'_{2i} = a_1 + a_2 X_{1i} + a_3 Y_{1i} + \sum_{j=1}^n w_j U(|(X_{1j}, Y_{1j}) - (X_{1i}, Y_{1i})|) \quad (8)$$

347 where  $U(r) = r^2 \log r^2$  and  $|(X_{1j}, Y_{1j}) - (X_{1i}, Y_{1i})|$  is the Euclidean distance between both points  
 348  $(X_{1i}, Y_{1i})$  and  $(X_{1j}, Y_{1j})$ .

349

350 The coefficients  $(a_1, a_2, a_3)$  and  $w_j$  ( $j \in (1, \dots, n)$ ) are calculated to minimize a bending energy  
 351 function. The thin plate spline model is inspired by physical science. It uses a thin plate  
 352 distortion model under constraints applied at different spots. This model has the property of  
 353 defining the thin plate physical configuration which minimizes its bending energy. The idea is  
 354 to use this model to solve a bidimensional interpolation problem. Attempts are made to find  
 355 the function which permits the superimposition of the set of  $S_1$  points to the set of  $S_2$  points,  
 356 minimizing the needed bending energy as if the discards between homologous points of  $S_1$   
 357 and  $S_2$  had been applied orthogonally to the image plane - considered as a physical thin plate -  
 358 rather than to the image plane itself.

359 Write  $r_{ij} = |(X_{1i}, Y_{1i}) - (X_{1j}, Y_{1j})|$  for the distance between points  $i$  and  $j$  in  $S_1$ .

360

361 Bookstein (1989) defines the matrices:

$$K = \begin{bmatrix} 0 & U(r_{12}) & \dots & U(r_{1n}) \\ U(r_{21}) & 0 & \dots & U(r_{2n}) \\ \dots & \dots & \dots & \dots \\ U(r_{n1}) & U(r_{n2}) & \dots & 0 \end{bmatrix}, (n \times n);$$

$$P = \begin{bmatrix} 1 & x_1 & y_1 \\ 1 & x_2 & y_2 \\ \dots & \dots & \dots \\ 1 & x_n & y_n \end{bmatrix}, (n \times 3);$$

$$L = \begin{bmatrix} K & P \\ P^T & 0 \end{bmatrix}, (n+3) \times (n+3);$$

362

$$V = \begin{bmatrix} x'_1 & x'_2 & \dots & x'_n \\ y'_1 & y'_2 & \dots & y'_n \end{bmatrix}, 2 \times n;$$

$$Y = (V|0 \ 0 \ 0)^T, (n+3) \times 2;$$

$$W = (w_1, \dots, w_n);$$

363 The equation

$$364 \quad L^{-1} Y = (W | a_1 \ a_2 \ a_3)^T$$

365 permits the computation of the functions  $\underline{f}$  and  $\underline{g}$  coefficients :

366

$$367 \quad \begin{cases} X'_{2i} = X_{2i}, \forall i \in (1, \dots, n) & (9) \\ Y'_{2i} = Y_{2i}, \forall i \in (1, \dots, n) & (10) \\ \sum_{i=1}^n w_i = 0 \\ \sum_{i=1}^n X_{1i} w_i = 0 \\ \sum_{i=1}^n Y_{1i} w_i = 0 \end{cases}$$

#### 368 4.2.2 Evaluation of the model parameters

369

370 To obtain an accurate estimation of the transformation model parameters - polynomial or  
371 spline - it is necessary to find a large number of homologous points -e.g. 25 pairs of points for  
372 a degree 3 polynomial function- on both images to match. Generally, biologists seek to  
373 superimpose four serial cuttings on the reference one, which required 100 pairs for one set.  
374 This is very time consuming if done manually. To solve this problem, we have developed a  
375 method to find homologous points in images to match automatically.

376

377 Our goal in this step is to obtain homologous points, homogeneously distributed in the image  
378 to be sure to take all possible distortions into account. This step is completely automatic,  
379 therefore few erroneous couples of points are expected.

380 Based on these criteria, the algorithm is composed of the three following steps:

- 381 • primitive extraction in the images to match,
- 382 • matching of these primitives to generate homologous points,
- 383 • homologous points validation.

384

385

#### 386 4.2.2.1 Primitive extraction on the cuttings

387

388 There are two kinds of objects in our images: fiber sections and the interfiber network.

389 Intuitively, when the operator is searching interactively for homologous points, he very often

390 selects intersections of branches belonging to the interfiber network. Consequently, our idea is

391 to extract the intersections automatically on both kinds of images: the reference cutting and

392 the cuttings to match on it.

393

394 Interfiber network extraction on the reference cutting has been explained in section 4.1. On

395 the other cuttings of the set, the available network information is made of thin branches - as

396 in the reference cutting - and transitions between uniform gray-level regions - see Fig. 2. A

397 recursive edge detection filter was used (Deriche 1987) which generates an image including

398 jumps of the gray level function. These jumps are particularly marked on thin branches and on

399 transitions between uniform gray level regions. This new image checks the main hypothesis

400 on which the interfiber network extraction on the reference cutting is based :

401 • the illumination intensity is homogenous on the whole image (because this image is the  
402 result of an edge detection filter),

403 • the available interfiber network information is composed of thin branches (because regions  
404 of different gray level intensities have been replaced by jumps between them).

405 Therefore, the same algorithm as for the reference cutting is used to obtain the available

406 interfiber network information in the edge detection image. On both kinds of images -

407 reference and the other cuttings - the triple points of the interfiber network skeleton which

408 define the center of the intersections are extracted. In the following, an intersection is defined

409 as a triple point of the interfiber network plus the three thin branches starting from it - 16

410 pixels long.

411

## 412 4.2.2.2 Matching pairs of homologous points

413

414 It is hypothesized that distortions between images can be locally assimilated to translations.

415 Then each intersection in the reference cutting is associated with a list of potential

416 homologous intersections in the cutting to match - see Fig. 9. These intersections are searched

417 in the cutting to match in a window of 64 x 64 pixels centered on the reference cutting

418 intersection - i.e. the triple point (x,y) position. To find accurate matching, two kinds of

419 information are applied : the intersection shape and the compatibility with distortion

420 information, available around the analyzed reference cutting intersection.

421

422 A shape criterion based on the calculus of the differences between matched branches has been

423 defined - see Fig. 10 -. This criterion is sensitive to angular and shape differences between

424 branches. Calling O - resp. O' - the triple point of the considered intersection in the reference

425 cutting - resp. the cutting to match - and (B<sub>1</sub>, B<sub>2</sub>, B<sub>3</sub>) - resp. (B'<sub>1</sub>, B'<sub>2</sub>, B'<sub>3</sub>) - its branches, O426 and O' are superimposed and for each couple of matched branches (B<sub>i</sub>, B'<sub>i</sub>), the sum of the

427 square differences of the pixel coordinates is calculated :

$$428 \quad d_i = \sum_{k=1}^{\min(L(B_i), L(B'_i))} \text{dist}_8(P_k \in B_i, P'_k \in B'_i)^2$$

429 with L(B<sub>i</sub>) - resp L(B'<sub>i</sub>) - the length of branch B - resp. B' - and dist<sub>8</sub> the D<sub>8</sub> distance (so-430 called chessboard distance) between P<sub>k</sub> (P<sub>k,x</sub>, P<sub>k,y</sub>) and P<sub>k</sub> (P'<sub>k,x</sub>, P'<sub>k,y</sub>) - is defined as :

$$431 \quad \text{dist}_8(P_k, P'_k) = \max (|P_{k,x} - P'_{k,x}|, |P_{k,y} - P'_{k,y}|).$$

432 This calculus is normalized - d<sub>i</sub> / n ← d<sub>i</sub> where n = min (L(B<sub>i</sub>), L(B'<sub>i</sub>)) - and iterated on the

433 three branches:

434 
$$d = \sum_{i=1}^3 d_i$$

435 In a first approximation, it is considered that the right solution corresponds to the couple of  
 436 intersections which minimizes  $\underline{d}$ . But the direct use of this criterion produces a large number  
 437 of errors because genuine matching is sometimes a secondary minimum of this similarity  
 438 function. To enhance this result, the decision process includes available information about the  
 439 local distortion in the analyzed intersection neighbourhood. For each intersection to match, a  
 440 probability is associated with each potential matching using the similarity criterion. If in the  
 441 neighbourhood of the intersection, many potential matchings in a given direction with a great  
 442 probability are found, the matching probability in this direction for the analyzed intersection is  
 443 enhanced and the matching probability in the orthogonal direction is reduced. To implement  
 444 this idea, a relaxation process inspired by Barnard and Thompson (1980) was used defining a  
 445 probability initialisation, a neighbourhood interaction function and an iteration process.

446

447 For a considered intersection  $\underline{i}$  in the reference cutting, an initial probability is associated with  
 448 each potential matching intersection  $\underline{l}$  in the cutting to superimpose.  $W_i(l)$  is termed :

449

450 
$$w_i(l) = \frac{1}{1 + s_i(l)}$$

451

452 Let  $p_i^0(l^*) = 1 - \max_{l \neq l^*} (w_i(l))$  be the initial probability of « no matching » for the intersection

453 i. Baye's rule is applied to obtain an initial estimate of the probability associated with label  $l$ :

454

$$455 \quad p_i^0(l) = p_i(l/i) \times (1 - p_i^0(l^*))$$

$$456 \quad \text{with } p_i(l/i) = \frac{w_i(l)}{\sum_{l \neq l^*} w_i(l)}$$

457 and  $l^*$  non matching label

458 Two neighbourhoods are considered :

459 • A spatial neighbourhood to select intersections:

460  $j$  is the neighbour of  $i$  - ie  $j \in V(i)$  - if  $\max(|x_i - x_j|, |y_i - y_j|) \leq D_{\text{spatial}}$

461 • A label neighbourhood:  $l'$  is a neighbour of  $l$  if  $\max(|l_x - l'_x|, |l_y - l'_y|) \leq D_{\text{label}}$ .

462  $l_x$  and  $l'_x$  - resp.  $l_y$  and  $l'_y$  - are the vectors joining the considered pair of intersections to

463 match in  $x$  -resp.  $y$  - direction.

464

465 Two interaction coefficients are computed :  $q^+$  which measures the compatible matchings in

466 the neighbourhood and  $q^-$  the incompatible ones. These are defined as follows:

$$467 \quad q_i^{+k}(l) = \sum_{j, j \neq i, j \in V(i)} \left[ \sum_{l' \in \text{neighbour}(l)} p_j^k(l') \right] \quad \text{for } l \neq l'$$

$$q_i^{-k}(l) = \sum_{j, j \neq i, j \in V(i)} \left[ \sum_{l' \notin \text{neighbour}(l)} p_j^k(l') \right] \quad \text{for } l \neq l'$$

468 where  $k$  represents the iteration step.

469

470

471 The final interaction coefficient is:

$$472 \quad q_i^k = \frac{q_i^{+k}}{1 + q_i^{-k}}$$

473

474 The initial probabilities are updated at each step using the interaction coefficient:

475

$$476 \quad p_i^{k+1}(l) = p_i^k(l) \times [A + B \times q_i^k(l)]$$

477

478 where A is the regulation factor - fixed to 0.0025 - and B controls the updating speed - fixed  
479 to 2.5 -. Then, the probabilities are normalised:

480

$$481 \quad p_i^{k+1}(l) = \frac{p_i^{k+1}(l)}{\sum_{l'} p_i^{k+1}(l')}$$

482

483 The relaxation is processed until stabilisation, reached generally after 10 iterations -see Fig.  
484 11. The couple of matched intersections associated with the best probability is then selected  
485 but will be validated in the next step.

486

#### 487 4.2.2.3 Validation of pairs of homologous points

488

489 The matching process generates a large number of homologous points on most images to  
490 superimpose on the reference cutting - between 100 and 300 -. These points are used to  
491 evaluate the geometrical transformation model coefficients - polynomial or spline. Models are  
492 very sensitive to erroneous homologous points - especially the polynomial model, see Fig. 12.



493 Therefore, it is important to check the relevance of homologous points obtained by the  
494 automatic process. Three criteria are applied to filter the homologous points:

495

- 496 1. Only homologous points with 0.8 matching probability score are selected.
- 497 2. Only around 100 homologous points uniformly distributed on the whole image are retained  
498 to be sure of taking into account all possible distortions.
- 499 3. The relevance of homologous points to the polynomial model is analyzed. In a first  
500 approach (Buche and Camillerapp (1991)), we eliminated aberrant homologous points  
501 according to the residues using the least squares method. If these residues were higher than  
502 a given threshold - computed according to the residues' standard deviation - we suppressed  
503 the homologous points pair corresponding to the largest residue. Then, the polynomial  
504 coefficients and residues were recalculated to detect other aberrant couples. This method is  
505 not very robust and is valid only if there are few aberrant homologous points. For this  
506 reason, a filter inspired by a robust regression method called the least-median-of-squares  
507 method was implemented - LMedS - (Meer et al (1991)) instead of the least squares  
508 method.

509

510 The goal of this method is to identify outliers in data, that is, points greatly deviating from the  
511 model. LMedS is a method that remains reliable if less than half of the data are contaminated.

512

513

514 In this method, the parameters are estimated by solving the nonlinear minimization problem:

$$515 \quad \min_{1 \leq i \leq n} \mathit{med} r_i^2$$

516 where *med* means the median value and

$$517 \quad r_i^2 = (X'_{2_i} - X_{2_i})^2 + (Y'_{2_i} - Y_{2_i})^2$$

518 where  $(X_{2_i}, Y_{2_i}) \in S_2$ ;  $(X'_{2_i}, Y'_{2_i}) \in S'_2$  as defined by Eq. 2 and 3.

519 The time-complexity of the basic algorithm is very high. If  $\underline{n}$  is the number of homologous  
 520 points and  $\underline{p}$  the number of polynomial model coefficients, then the complexity is  
 521  $O(n^{p+1} \log n)$ , which is prohibitively large. Use was made of a random-sampling version of  
 522 the algorithm which reduces the time-complexity to  $O(\underline{m} \log n)$  where  $\underline{m}$  is the number of  
 523  $\underline{p}$ -tuples chosen randomly.

524

525 The probability  $\underline{P}$  that all  $\underline{m}$  different  $\underline{p}$ -tuples chosen at random will contain at least one or  
 526 more outliers is :

$$527 \quad P = 1 - \left[ 1 - (1 - \varepsilon)^p \right]^m$$

528 where  $\varepsilon$  is the fraction of data contaminated by outliers. For instance, for  $\underline{p} = 3$ ,  $\underline{m} = 100$ ,

529  $\varepsilon = 0.5$ ,  $P = 1.59 \times 10^{-6}$ , which is a very low probability.

530

531 The robust estimate of the standard deviation is:

$$532 \quad \hat{\sigma} = 1.4826 \times \left[ 1 + \frac{5}{n-p} \right] \mathit{med}_{1 \leq i \leq n} \sqrt{r_i^2}$$

533 Based on the robust LMedS model and the standard deviation estimate, homologous pairs of  
 534 points  $\{(X_{1_i}, Y_{1_i}) ; (X_{2_i}, Y_{2_i})\}, i \in (1, \dots, n)$  are filtered as follows:

535 1. binary weights  $\underline{w}_i$  are associated with each homologous pair of points

536

$$537 \quad w_i = \begin{cases} 1 & \text{if } \frac{|r_i|}{\hat{\sigma}} \leq 2.5 \\ 0 & \text{if } \frac{|r_i|}{\hat{\sigma}} > 2.5 \end{cases}$$

538 2. homologous pairs having  $\underline{w}_i = 1$  are considered as belonging to the assumed model,

539 homologous pairs having  $\underline{w}_i = 0$  are considered as outliers.

540

## 541 **5. Results**

542

543 This section presents the results obtained from two kinds of muscle, chicken and pork. First,  
 544 the different steps of our method were applied to 20 cutting sets of chicken muscle (i.e 3763  
 545 fibers) made of 2 cuttings: 1 reference and 1 typing coloration -ATPase. Second, the method  
 546 was applied to 20 cutting sets of pork muscle (i.e 3252 fibers) made of 3 cuttings: 1 reference  
 547 and 2 typing colorations - ATPase and SDH.

548

### 549 **5.1 Time consumed per set**

550

551 The average number of fiber sections per cuttings set is 163 for pork muscle and 188 for  
 552 chicken muscle. For pork, there are two cuttings to match on the reference, therefore the  
 553 respective following correction times are referred to as b1 and b2. The complete processing

554 time includes automatic processing time plus interactive correction time. The results are  
555 presented in Table 1.

556

## 557 5.2 Error rates

558 The erroneous or missing branches rate is a mean rate obtained by dividing the number of  
559 erroneous or missing branches by the total number of branches for each reference cutting. The  
560 erroneous homologous points rate is obtained by dividing the number of erroneous  
561 homologous points - deleted by the operator - by the total number of automatically found  
562 homologous points. The added homologous points rate is the number of homologous points  
563 interactively added by the operator -in the fiber following step- divided by the total number of  
564 homologous points. The results are presented in Table 2.

565

## 566 5.3 Accuracy in the following step

567

568 The distortion models -splines and polynomial- are efficient and complementary because most  
569 of the distortions encountered are correctly estimated using one of these models. The kind of  
570 distortion in the image leads to the model choice:

571

- 572 • Case 1: one or two local distortions in the image

573 In this case, if the homologous points are uniformly distributed in the image, the  
574 polynomial model gives a good estimation of the distortion. It has been shown in Buche  
575 and Camillerapp (1991) that a degree 3 polynomial model gives the best precision. The  
576 model precision is defined as the standard residual deviation - measured in pixels - of the  
577 homologous points. 4.43 pixels on x-axis were obtained and 4.15 pixels on y-axis. Fig. 13

578 shows an example which illustrates the typical use of a polynomial model. A little  
579 distortion is taken into account in the upper right corner of the image.

580

581 Unlike the polynomial model, the homologous points density must be higher for the spline  
582 model. Therefore, this model is not advised for small distortions because the operator has  
583 to add more homologous points interactively than with the polynomial model.

584

585 • Case 2: several local distortions in the image

586 It can be noted first that spline model offers a greater degree of liberty than the polynomial  
587 one to fit local distortions. Second, it is certain the homologous control points belong to the  
588 estimated network - cf. eq. 9 and 10. Thirdly, the network can be locally distorted by  
589 adding locally several homologous points- without disturbing superimposition in the  
590 neighbouring zones -in opposition to the polynomial model. Fig. 14 and 15 present a  
591 typical case when using the same set of control points, the thin plate spline model is clearly  
592 better than the polynomial one to fit local distortions. The costs of these improvements are:

593

- 594 1. the homologous points density -especially in the distortion zone- must be high to fit all  
595 the local distortions,
- 596 2. the processing time is higher for the spline model (about 30 seconds) than for the  
597 polynomial one. The performance had been estimated on a Sun Sparc 4/75 Station.

598

599

## 600 5.4 Results interpretation

601

### 602 1- Network extraction step

603

604 Interfiber network interactive validation time and erroneous branches rates come up to  
605 biologists' expectations. However, the worse rate for chicken muscle may be explained by the  
606 presence of different noises -ignored in our model hypothesis. These noises are the results of  
607 cuttings, chemical treatments and image acquisition steps:

- 608 • Fiber sections and the interfiber network are not homogeneous in grayscale -resulting in  
609 coloration problems. Therefore, in the thresholding step, fiber sections and the interfiber  
610 network are not well detected.
- 611 • During the image acquisition stage, the illumination was not homogeneous on all the field  
612 area. This problem comes from bad thresholding.
- 613 • Fiber sections contain characterized freezing points which appear in white on the image -  
614 the same luminance as the interfiber network. This case does not disturb the thresholding  
615 because, after this step, the algorithm eliminates components which are not connected to  
616 the interfiber network. But it disturbs the long distance closings. Indeed, the dynamic  
617 programming process keeps the lanes maximizing the accumulated luminance intensities.  
618 The freezing points appear in this image and then induce erroneous closing branches.

619

620

621 2- Fiber section following step

622

623 The matching process gives satisfactory results:

- 624 • The low rates of erroneous homologous points prove that the robust regression method is  
625 an efficient filter after relaxation process,
- 626 • The low rates of added homologous points prove that the used primitives -intersections -  
627 are significant. Indeed, these primitives permit the matching method to find many well-  
628 distributed homologous points in the entire image.

629

630 However, as in network extraction step, the results are less satisfactory in this step for some  
631 sets of chicken muscle compared to pork. The reason is that in some chicken cuttings to  
632 match, there is less interfiber information than in swine cuttings. Therefore, the algorithm  
633 finds fewer intersections. For the relaxation process, the lower the number of intersections,  
634 the higher the probability of obtaining badly-matched intersections.

635 Our method was initially developed for pork muscle fibers. Consequently, the results are  
636 better for this muscle than for that of chicken. But, our method has been judged robust enough  
637 to be used on several types of muscle, such as trout, beef, rabbit, mutton or turkey.

638

639 5.5 Two examples of biological results obtained with this method

640

641 This section introduces two concrete biological applications of our method, which underline  
642 two of its significant qualities. The first one, coming from animal genetic selection, shows that  
643 the degree of method automation allows work on a very large number of samples. The second  
644 one, coming from meat quality control, illustrates that it is possible with this method to  
645 analyze different parameters on the fibers simultaneously.

646  
647  
648  
649  
650  
651  
652  
653  
654  
655  
656  
657  
658  
659  
660  
661  
662  
663  
664  
665  
666  
667  
668  
669

### 5.5.1 Comparison analysis of selected lines of chicken

Two lines of chickens sharing the same genetic origin were studied (Remignon 1993): one fast and one slow-growing. The aim of the study was the analysis of the influence of selection on the total number of fibers, myofiber types and cross-sectional areas of the different fiber types.

The experimental sampling was designed as follows:

Three muscles were studied: pectoralis major is a muscle mainly composed of glycolitic fibers; anterior latissimus dorsi is mainly composed of oxidative fibers and sartorius is a mixed muscle composed of oxidative and glycolitic fibers. Samples have been taken at 6 ages (0, 1, 3, 5, 11, 55 weeks), on twelve animals per age and per line. Three fields - 250 fibers - have been analysed per muscle, animal and age. The total number of analysed fibers was therefore around 324 000 fibers.

Different results were obtained:

1. There is a higher total number of fibers (+20%) for the fast-growing line in anterior latissimus dorsi.
2. At hatching, cross-sectional areas of the different fiber types are the same. After one week, fibers are twice as large in the fast-growing line. Thereafter, during growth, the difference remains constant between the two lines.
3. The myofiber type distribution was the same in the two selected lines.



670 Therefore, it seems that genetic selection for the divergent growth rates modifies the  
671 quantitative but not qualitative properties.

672

### 673 5.5.2 Meat quality control of pork muscles

674

675 The aim of this study (Fernandez 1993) was to observe the fall in pH in slaughtered animal's  
676 muscles, because this has a great influence on meat quality parameters like colour, water-  
677 holding capacity and tenderness. The fall of pH is mainly determined by muscle glycogen  
678 content after slaughtering. Therefore, the precise objectives were the study of the effect of a  
679 24h-fasting and behavioral stress (meetings of pairs of animals) on glycogen variation.

680 Two muscles were studied: longissimus dorsi (a muscle mainly glycolitic) and semispinalis (a  
681 muscle mainly oxidative). Measures were carried out on subsamples coming from the same  
682 samples at two levels:

- 683 • a global level, using an enzymatic method on muscle homogenates
- 684 • a detailed level, using histology and our image analysis method on muscle fibers.

685 The first result is a glycogen contents comparison between the two muscles using both  
686 methods - at global and detailed levels - In Fig. 16 are shown the contents of glycogen,  
687 measured in micromole per gram of fresh tissue, using the global level method. Fig. 17 shows  
688 the average luminance intensities measured on glycogen stainings using our detailed level  
689 method. The higher the luminance, the lower the rate of glycogen in the fiber. Comparing  
690 those results, a generally high level of concordance can be observed.

691

692 The second one (Fernandez et al (1994)) is an analysis of both factors - fasting and stress  
693 effects - depending on the fiber types. These original results could only be obtained at the  
694 detailed level using our method. In Fig. 18 (resp. Fig.19), four groups of average luminance

695 intensities are represented, measured on glycogen stainings for longissimus dorsi muscle  
696 (resp. semispinalis muscle). The first column is the total number of fibers and the three others  
697 represent the three fiber types considered ( $\alpha$ R,  $\alpha$ W and  $\beta$ R). R (for red) represents oxidative  
698 fiber type. W (for white) represents glycolitic fiber type. Subtypes for red fibers indicate the  
699 contraction speediness of fibers ( $\alpha$  for fast and  $\beta$  for slow). The area percentages for each type  
700 of fiber are also given under the figures for each group.

701 ATP regeneration is faster in glycolitic fibers than in oxidative fibers. On the contrary,  
702 oxidative fibers are more efficient than glycolitic ones in the total amount of ATP made for  
703 one quantity of glycogen. For this reason, a red muscle like semispinalis, mainly composed of  
704 oxidative fibers, plays an important function in posture and movements under the position of  
705 rest, by contrast with glycolitic muscle like longissimus dorsi, which is mainly recruited  
706 during acute physical response. This is the reason why during fasting, semispinalis has to rely  
707 on its endogeneous substrates, glycogen, more than longissimus dorsi. This interpretation is  
708 consistent with the fact that in longissimus dorsi, there is also a trend toward an increase in  
709 glycogen luminance in red fibers ( $\alpha$ R and  $\beta$ R).

710

711 As for stress effect, results are different in both muscles. In longissimus dorsi, there is a  
712 significant effect for fasted animals but not for fed animals especially in fast twitch fibers ( $\alpha$ R  
713 and  $\alpha$ W), which are the most active fibers during physical activity associated with aggressive  
714 interaction between animals. In semispinalis, there is also a significant effect for fed animals  
715 in fast twitch fibers and no effect on fasted animals.

716

717 To conclude with these results, we can say that the use of our method allows further  
718 examination at the fiber type level and not only at the global level.

719

## 720 6. Discussion

721

### 722 6.1 Interfiber network extraction

723 • In rare cases, the interfiber network result is completely erroneous. It happens for example  
724 when the background is not homogeneous. It is difficult to find a completely automatic  
725 algorithm able to generate optimal results for all types of muscles and cutting preparations.

726 It was therefore decided to develop an interactive tool which contains classical and  
727 morphological operators -lowpass and highpass filters, opening and closing, tophat, global  
728 interactive thresholding ...- plus specific parts of the extraction step algorithm - thinning,  
729 short distance closing .... This toolbox is used in an interactive mode when the operator  
730 judges that it will be more rapid to extract the interfiber network using it rather than to  
731 correct the automatic result.

732 • At present, in order to make restitution of the interfiber network thickness, dilatations are  
733 applied on the interfiber skeleton and merged with the big structure image - an  
734 intermediate image stored after image thresholding in the automatic extraction step.  
735 Unfortunately, the result is not very accurate for two reasons. First, branch thickness is not  
736 homogeneous. Therefore homogeneous dilatation of the interfiber skeleton is not sufficient.  
737 Second, the gray level in the interfiber network is sometimes not homogeneous - due to  
738 freezing points for instance. Therefore, the big structure image is not useful because too  
739 many freezing points appear as belonging to the interfiber network. It would seem likely  
740 that a region growing algorithm -starting from the thin branches and stopping on gray level  
741 intensity jumps- will improve the restitution of interfiber network thickness.

742

### 743 6.2 The choice of the transformation model

744

745 In the case of large-scale local distortions, the poor results of the polynomial model led us to  
746 test a more appropriate one. Two approaches were considered :

- 747 • The first idea, inspired by the Adaptative Mapping algorithm -Flusser (1991)- was to  
748 subdivide the image into several regions -the subdivisions depending on local distortions-.  
749 In each region, the algorithm calculates a polynomial distortion model. After several tests,  
750 it was noted that the Adaptative Mapping algorithm generates on our class of images large  
751 scale discontinuities on region boundaries. Therefore, this method was rejected.
- 752 • The second idea was the Bookstein (1989) algorithm based on spline functions. The very  
753 interesting property of this model is the preservation of spatial continuity between regions  
754 of local distortions.

755

756

### 757 6.3 Fibers following

758

759 At present, the shape criteria used in the relaxation algorithm concern only translations.  
760 Sometimes, we observe fiber distortions including rotations. To improve the results of our  
761 algorithm, a local polynomial model will be tested to match the intersections instead of the  
762 translation model. In the relaxation method, a label will be associated with a polynomial  
763 function -instead of a vector. It will be necessary to minimize another similarity criterion  
764 between two polynomial functions of the same degree.

### 765 **7. Conclusion**

766

767 At present, the RACINE software is successfully used in a routine fashion by several  
768 laboratories on two kinds of muscle, pork and chicken, and gives promising results for rabbit  
769 and turkey. Positive tests have been obtained for mutton, trout and beef. The software presents  
770 strong advantages:

- 771 • firstly, it permits biologists to obtain easily in a semi-automatic way, several structural  
772 parameters characterizing each fiber section,
- 773 • secondly, thanks to its matching reliability, the software gives for each fiber section precise  
774 information extracted from cuttings to match regarding fiber types and luminances,
- 775 • thirdly, the main contribution of RACINE is that its semi-automatic aspect permits  
776 application of this software to several thousands of fiber sections, which allows reliable  
777 statistical analysis.

778

779 We think also that the localization of the computed data delivered by our software would help  
780 biologists to analyze spatial distributions of fiber types, for example, small fibers in trout  
781 muscles, which appear after hatching. Therefore, it can be interesting to analyze the spatial

782 distribution of fibers according to their size distribution. The biological aim is to analyze the  
783 relationship between the interfiber network texture and meat quality, tenderness for instance.

784

785 At present, for trout muscle, our software is used to follow small fiber growth after hatching.  
786 Indeed, a special semi-automatic tool has been developed based on our fiber following  
787 algorithm which permits scientists to observe the appearance or disappearance of fiber  
788 sections between two serial cuttings.

789

790 Our work will now consist in improving some parts of the software (see 6.1 and 6.3). Our goal  
791 is also to generalize the matching process -using other primitives like high curvature points-,  
792 in order to use it on other image classes for other kinds of applications as for example the  
793 matching of satellite images.

794

#### 795 **Acknowledgements**

796 The authors wish to express their gratitude to the French National Institute of Agronomic  
797 Research and especially to the Computer Sciences Department which made funds available  
798 for this project.

799

#### 800 **References**

801

802 Ashmore, C.R. and Doerr, L. (1971) Comparative aspects of muscle fiber types in different  
803 species. *Exp. Neurol.*, 31:408-418.

804

805 Barnard, S.T., Thompson, W.B. (1980) Disparity analysis of images. *IEEE Transactions on*  
806 *Pattern Analysis and Machine Intelligence*, Vol PAMI-2, n°4, July 1980: 333-340.

- 807
- 808 Bookstein, F.L. (1989) Principal warps: thin-plate splines and the decomposition of  
809 deformations. IEEE Transactions on PAMI, Vol. 11, n°6, June 1989: 567-585.
- 810
- 811 Brooke, M.H. and Kaiser, K.K. (1970) Muscle fiber types: how many and what kind ?. Arch.  
812 Neurol., 23:369-379.
- 813
- 814 Buche,P. and Camillerapp, J. (1991) Serial cutting matching: an application to muscle fiber  
815 characterization. Proc. Eurographics'91, edited by F.H. Post and W. Barth, published by  
816 Elsevier Science Publishers B.V., September 2-6, 1991, pp 329-340.
- 817
- 818 Bye, E; Gronnerod, O; Vogt, N.B. (1989) Multivariate classification of histochemically  
819 stained human skeletal muscle fibers by the SIMCA method. Histochemical Journal, 21:15-  
820 22.
- 821
- 822 Coster, M. and Chermant J.L. (1989) Précis d'analyse d'images, Presses du CNRS, pp360-  
823 380.
- 824
- 825 Deriche, R. (1987) Optimal edge detection using recursive filtering. Proc. First international  
826 conference on Computer Vision. London, June 1987, edited by J.M. Brady and A. Rosenfeld,  
827 published by the IEEE Computer Society Publications Office.
- 828
- 829 Dudley, J.; Dayhoff, M.; Ledley, C. (1983) Muscle biopsy data acquisition and display. Proc.  
830 7th annual symposium on Computer Applications in Medical Care, October 1983, pp 763-  
831 766. Edited by J. T. O'Neill, published by the IEEE Computer Society Publications Office.

832

833 Fernandez, X.; Lefaucheur, L.; Candek, M. (1994). Comparative study of two classifications  
834 of muscle fibres. Consequences for the the photometric determination of glycogen according  
835 to fibre type in red and white muscle of the pig. Meat Science, Vol. 41 No. 2, pp 225-235.

836

837 Fernandez, X. (1993). Contributions à l'étude des facteurs de variation de la concentration  
838 musculaire en glycogène et du pH ultime chez le porc. Relations avec les qualités  
839 technologiques et organoleptiques de la viande. Thèse en Science des aliments de l'Université  
840 de Clermont-Ferrand. Avril 1993.

841

842 Flusser, J. (1991) A fast registration of images with complex geometric distortions. SCIA 91,  
843 vol II, pp 1011-1018.

844

845 Henckel, P. (1989) Image analysis, a rapid method to determine histochemical properties of  
846 skeletal muscles including individual types. Proc. 40th annual meeting of the European  
847 Association for Animal Production, Dublin. Edited and published by EAAP.

848

849 Jain, S. (1980). Segmentation of muscle cell pictures, a preliminary study. IEEE Transactions  
850 on PAMI. vol PAMI-2, no 3, p 232-243.

851

852 Kohler, R (1981) A segmentation system based on thresholding. Computer Graphics and  
853 Image Processing 15:319-338.

854



855 Marinova, S. , Lefaucheur, L., Fernandez X., Monin P. (1991). Relationship between  
856 metabolism and glycogen content in skeletal muscle fibers of large white and Hampshire  
857 crossbred pigs. *J. Muscle Foods*, 3, 91-97.

858

859 Meer, P; Mintz, D; Rosenfeld, A (1991) Robust regression methods for computer vision: a  
860 review. *International Journal of Computer Vision*, 6:1, 59-70.

861

862 Pernus, F ; Bjelogrljic Z. and Erzen, I (1986) A computer-aided method for muscle fiber type  
863 quantification. *Acta Stereol*, 5/1:49-54.

864

865 Pernus, F and Erzen, I (1991) Arrangement of fiber types within fascicles of human vastus  
866 lateralis muscle. *Muscle & Nerve*, 14:304-309.

867

868 Ranft, P., Prewitt, J. and Fu, K.S. (1983) Segmentation of microscopic transverse section  
869 pictures of muscle tissue using a split and merge technique. *Proceedings of the 6th*  
870 *International Conference on Pattern Recognition. Section 83, medical applications. pp 626-*  
871 *628. Edited by Marcelli Wein, published by the IEEE Computer Society Publications Office.*

872

873 Remignon, H. (1993) Contribution à l'étude histologique et biochimique des muscles dans  
874 deux lignées de poulets à croissance lente ou rapide. Thèse en Science des aliments de  
875 l'Université de Clermont-Ferrand. Décembre 1993.

876

877 Wong, Fu (1983) A parallel algorithm for muscle tissue images classification. *Proc. 7th*  
878 *annual symposium on Computer Applications in Medical Care, October 1983, pp 751-754.*  
879 *Edited by J. T. O'Neill, published by the IEEE Computer Society Publications Office.*



**Tables**

	Complete processing	Interfiber network correction	Following correction		Interactive correction
Chicken	17 min. 41 sec.	5 min. 09 sec. (a)	5 min. 58 sec. (b)		11 min 07 sec. (a)+(b)
Pork	14 min.	2 min. 39 sec. (a)	1 min. 25 sec. (b1)	2 min.24 sec. (b2)	6 min 28 sec. (a)+(b1)+(b2)

Table 1 : Time consumed per set

	Erroneous or missing branches rate in extraction step	Erroneous homologous points interactively removed rate in fiber following step		Homologous points interactively added rate in fiber following step	
Chicken	8,20 %	1,91 %		16,41 %	
Swine	4,76 %	0,12 %	0,63 %	2,45 %	2,35 %

Table 2 :Error rates. These results have been calculated comparing interactive correction of branches (resp. control points) to the branches (resp. points) number obtained after automatic interfiber network extraction (resp. homologous points extraction).

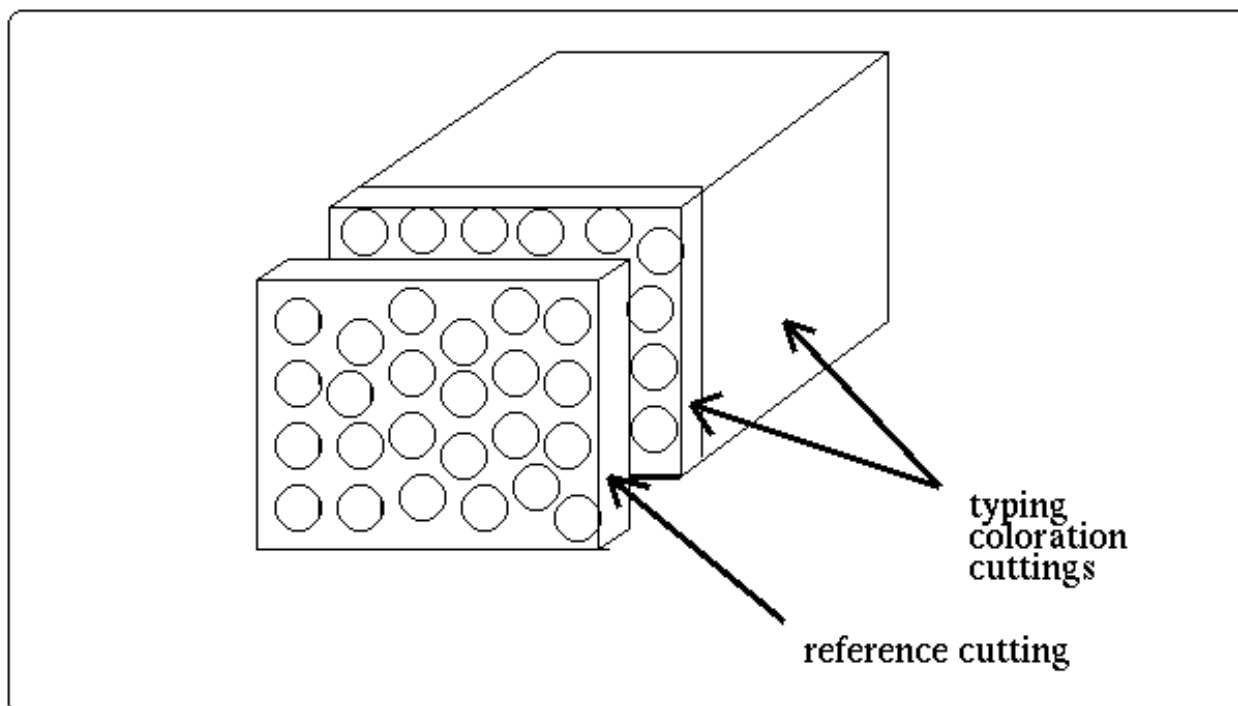
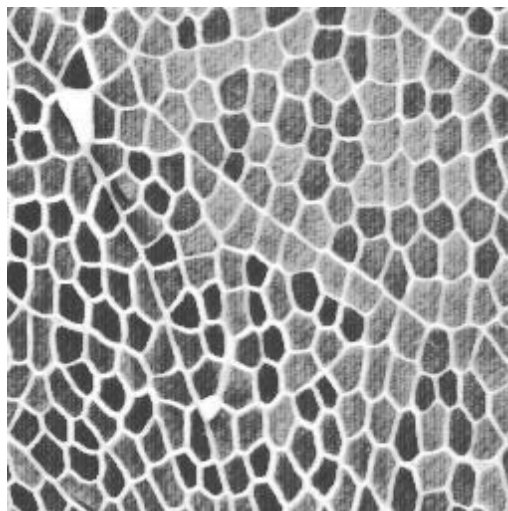
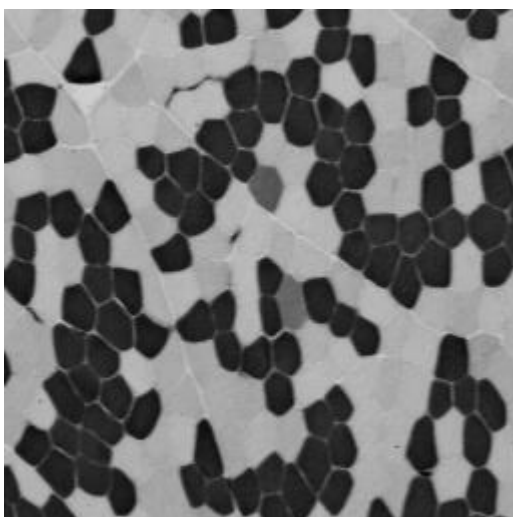
**Illustrations**

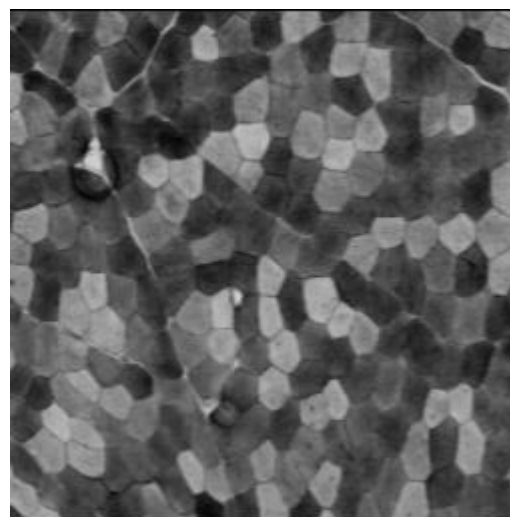
Fig. 1: Contiguous cuttings realized perpendicularly to the fiber length axis



(1)



(2)



(3)

Fig. 2: A serial cutting image set: the reference cutting (1), a typing cutting (2), a parameter cutting (3). The size of each image is 512 x 512 pixels.

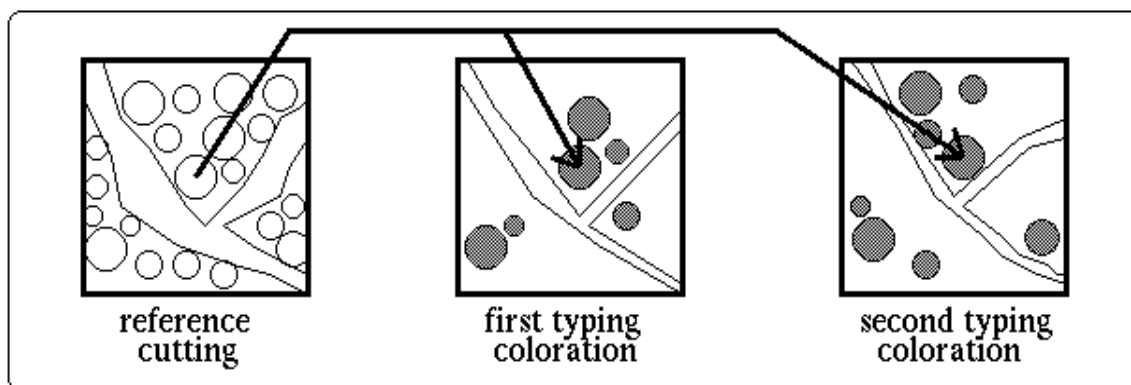


Fig. 3: Fiber following from the reference cutting to each cutting of the set

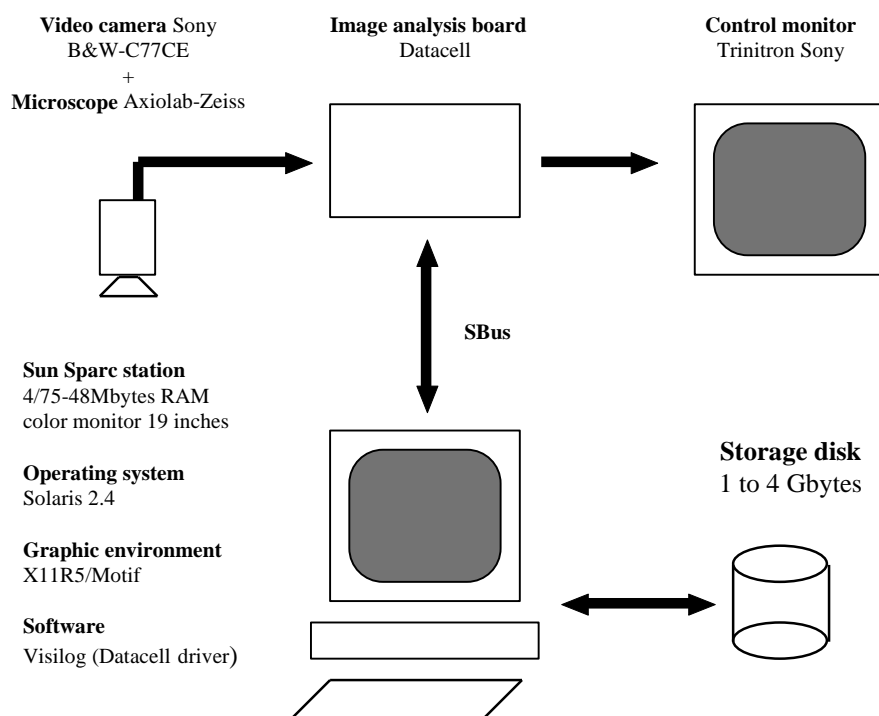


Fig. 4: Material platform required for using RACINE software.



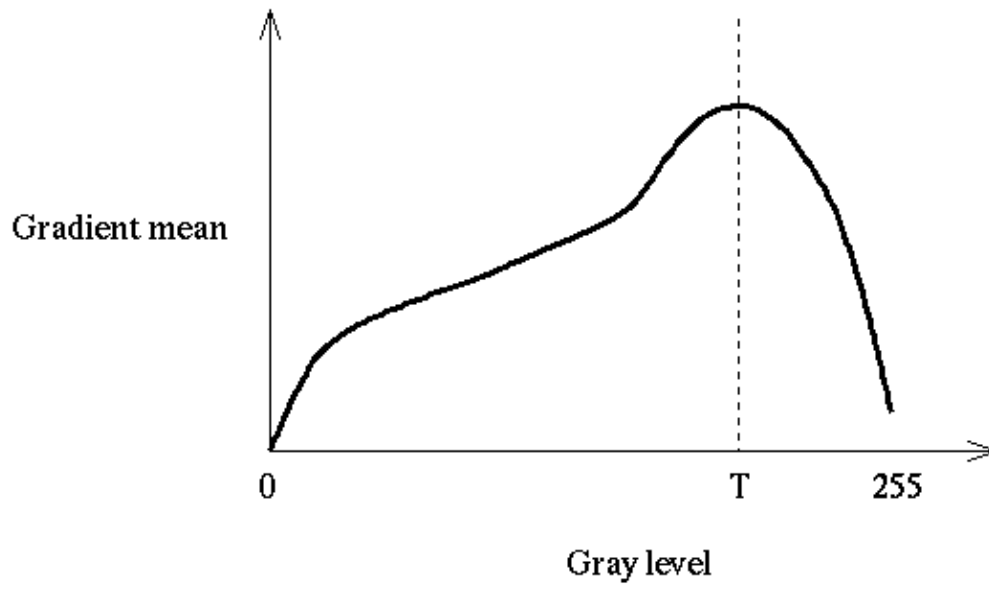


Fig. 5: Chosen threshold T in automatic extraction step.

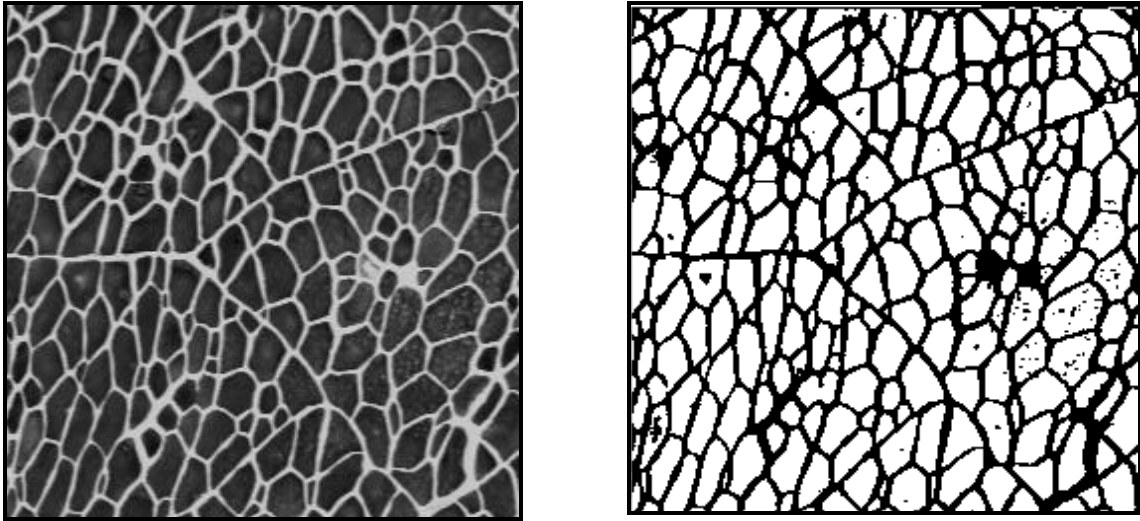


Fig. 6: Interfiber network (in white) in the initial gray level (left) image and in the binary (right) image (in black) after global automatic thresholding.  
The size of each image is 512 x 512 pixels.

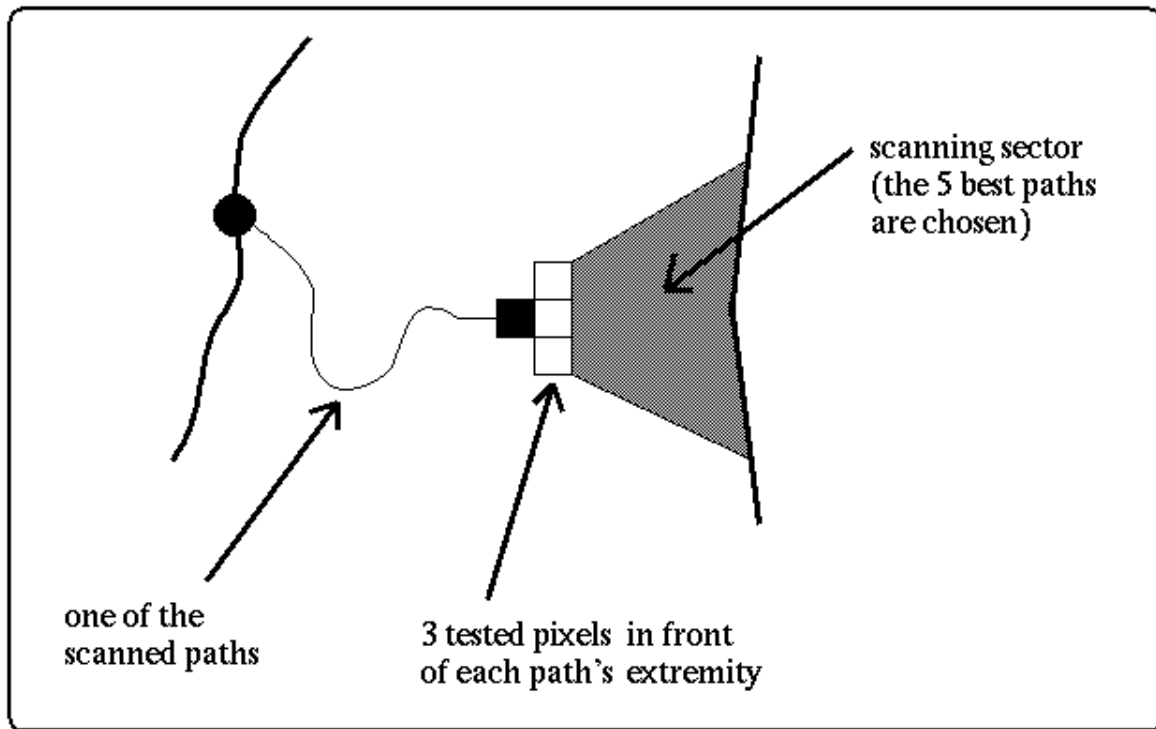


Fig. 7: Long distance branch closing step

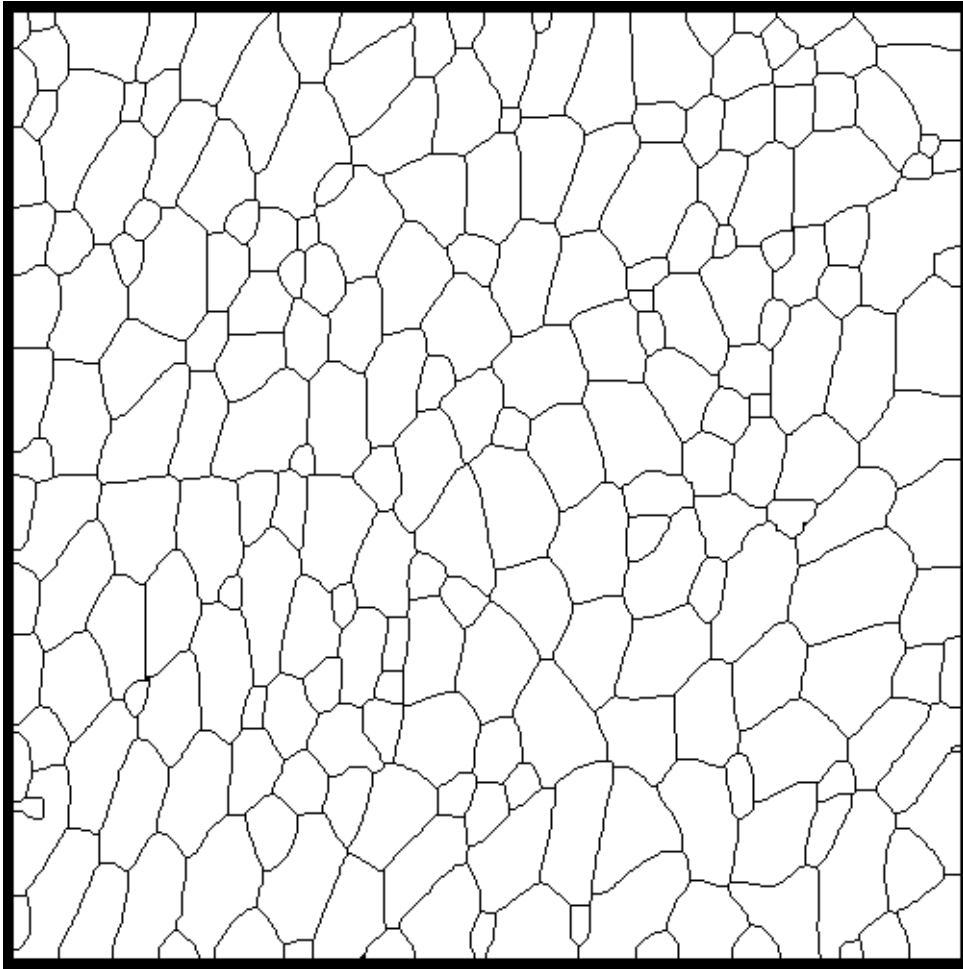


Fig. 8: Interfiber network final result - in black on the image -  
The original image is the reference cutting of Fig. 6. This result is superimposed on the original image to observe and correct the network (addition or omission).

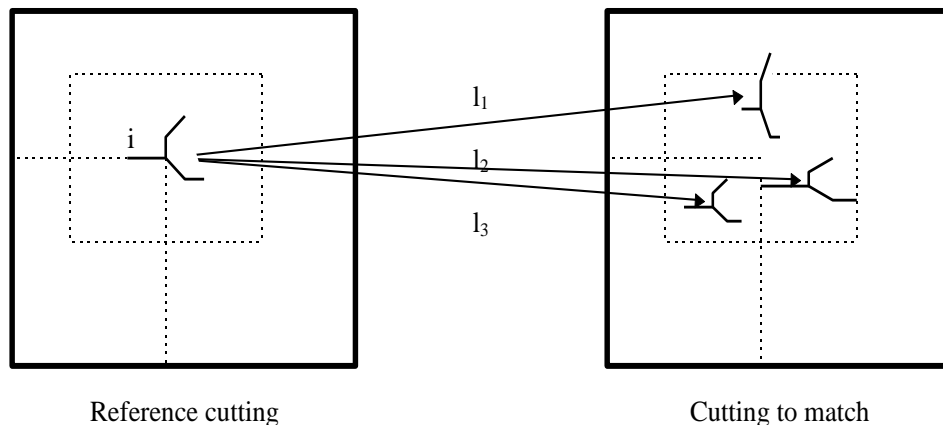


Fig. 9: The possible matchings  $l_1$ ,  $l_2$  and  $l_3$  for the intersection  $i$  - in the reference cutting - found in a  $64 \times 64$  pixels window - in the cutting to match- centered on the coordinates of the intersection  $i$ .

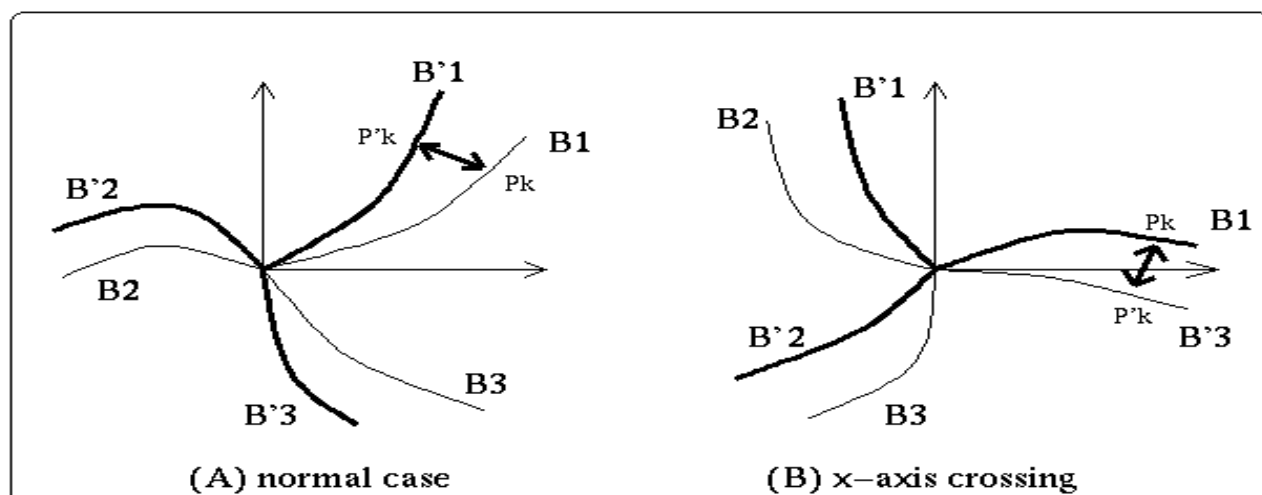


Fig. 10 : Similarity criterion between intersections.

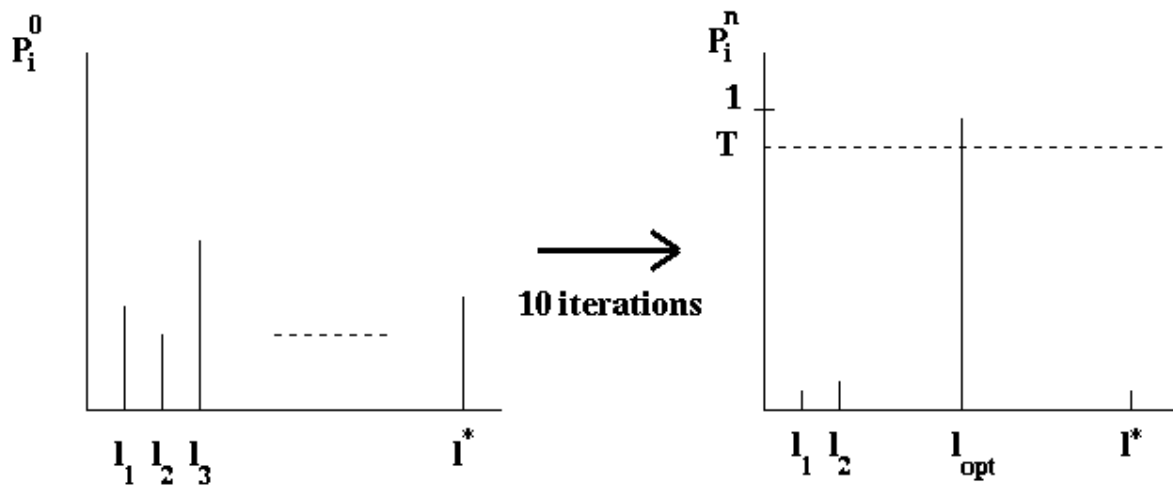


Fig. 11: Relaxation processing convergence toward  $l_{opt}$ .  
 The homologous pair of points corresponding to  $l_{opt}$  is selected if the matching probability score is superior to  $T$  ( $T=0.8$  in our algorithm).

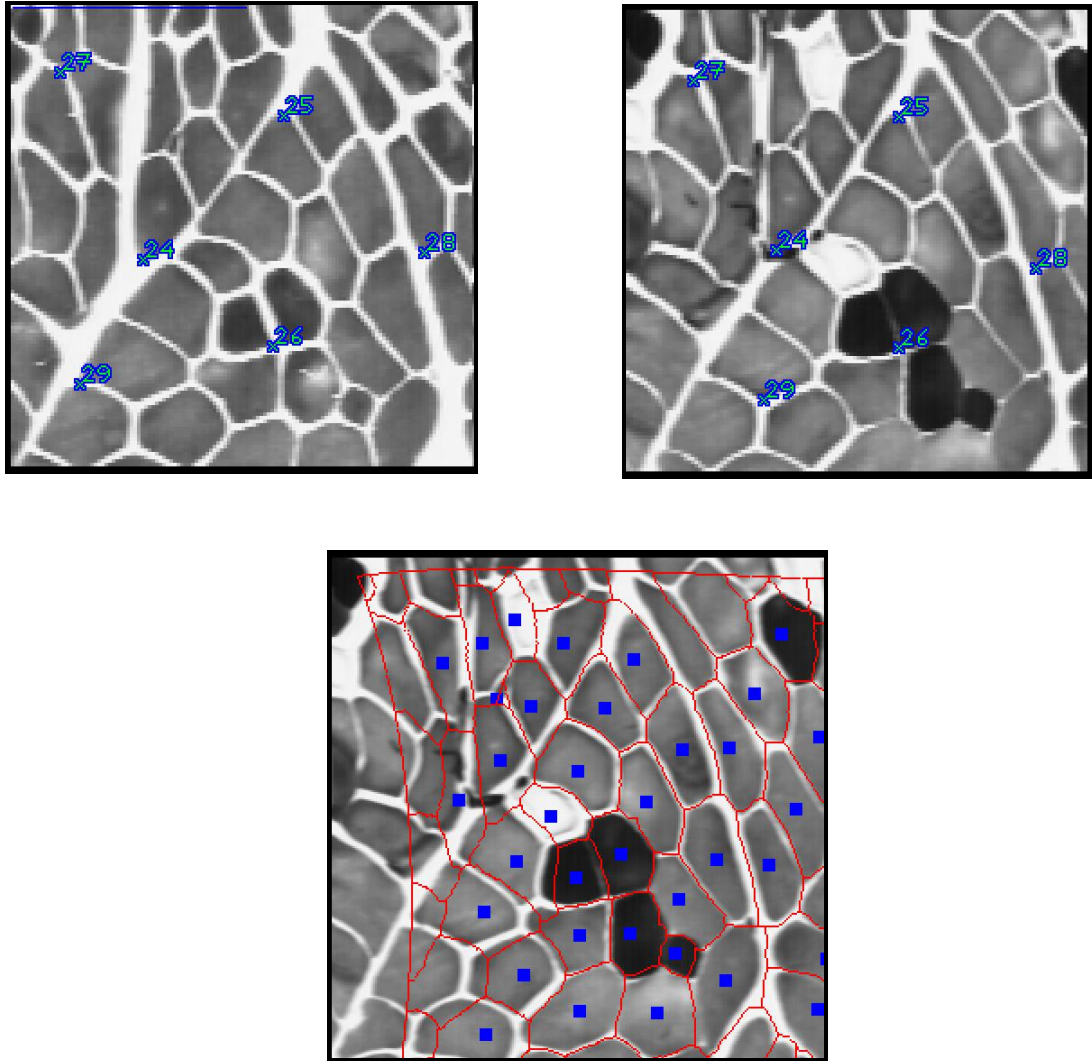


Fig. 12: The problem of polynomial transformation robustness: the interfiber network can be badly distorted by only a pair of erroneous homologous points (here control pair of points number 29)



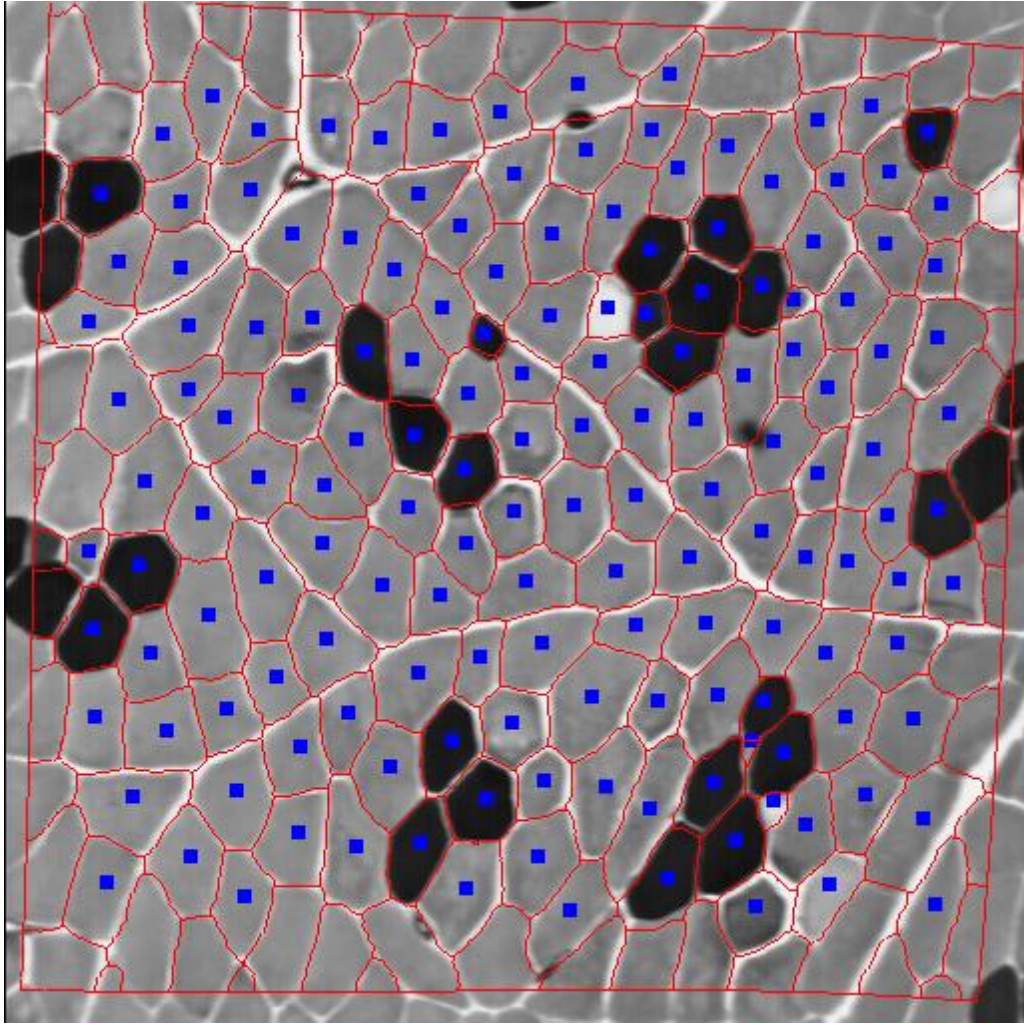


Fig. 13: Interfiber network superimposition on a cutting to match with a polynomial model

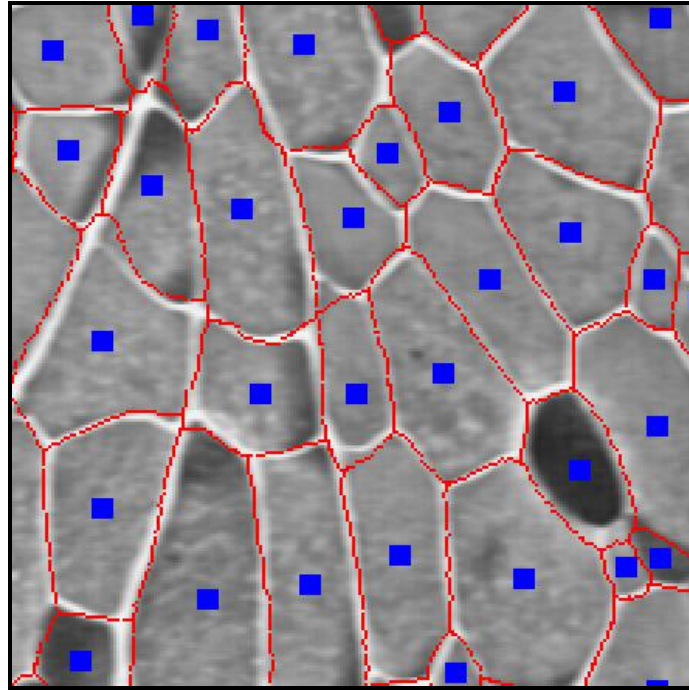


Fig. 14: Interfiber network superimposition on a cutting to match with a thin-plate spline model

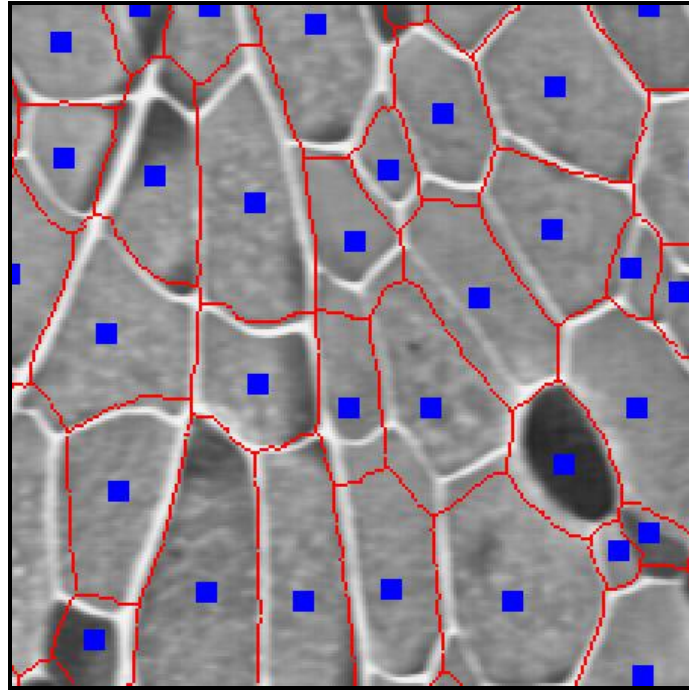


Fig. 15: Polynomial superimposition with the same control points set as in Fig. 14.  
The result is less accurate than with thin-plate splines

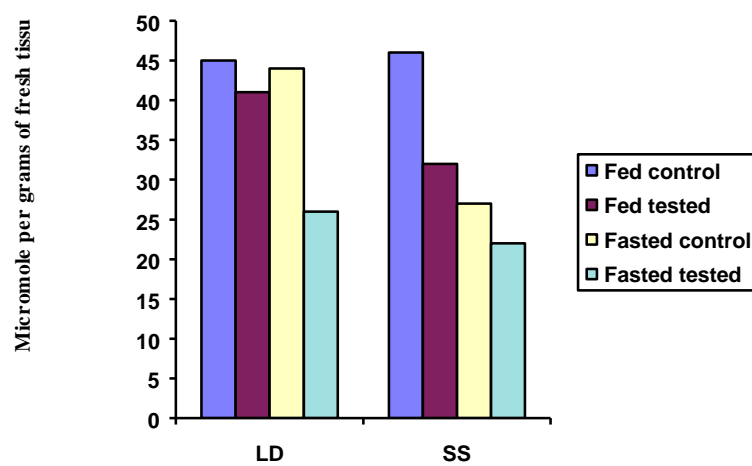


Fig. 16: Enzymatic determination of glycogen contents in Longissimus Dorsi (LD) and Semispinalis (SS) - given in micromole per gram of fresh tissue -

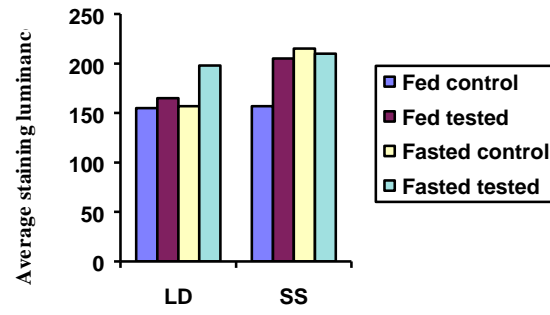


Fig. 17: Average luminance intensities measured on glycogen stainings in Longissimus Dorsi - LD - and Semispinalis - SS -

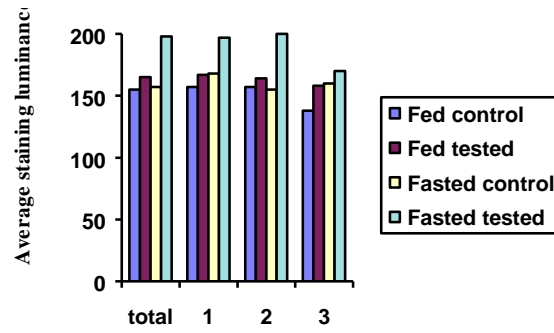


Fig. 18: Average luminance intensities measured on glycogen stainings in Longissimus Dorsi - LD - for the three types of fibers: (1)  $\alpha$ R, (2)  $\alpha$ W, (3)  $\beta$ R. The percentages of area are 14% for  $\alpha$ R, 77% for  $\alpha$ W and 9% for  $\beta$ R

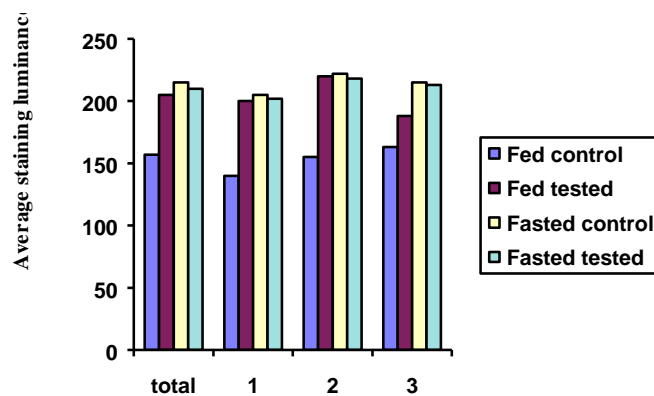


Fig. 19: Average luminance intensities measured on glycogen stainings in Semispinalis - SS - for the three types of fibers: (1)  $\alpha$ R, (2)  $\alpha$ W, (3)  $\beta$ R. The percentages of area are 19% for  $\alpha$ R, 42% for  $\alpha$ W and 39% for  $\beta$ R